

## RESEARCH ARTICLE

10.1002/2017JE005306

## Key Points:

- Hydrogen column densities upstream of Mars are inferred from charge exchange products of the solar wind measured in the upper atmosphere
- Hydrogen column density varies tenfold annually, implying comparable variability in escape flux, assuming a thermal Chamberlain exosphere
- Peak exospheric hydrogen densities occur at southern summer solstice rather than perihelion, suggesting a seasonal influence on escape

## Correspondence to:

J. S. Halekas,  
jasper-halekas@uiowa.edu

## Citation:

Halekas, J. S. (2017), Seasonal variability of the hydrogen exosphere of Mars, *J. Geophys. Res. Planets*, 122, doi:10.1002/2017JE005306.

Received 14 MAR 2017

Accepted 26 APR 2017

Accepted article online 2 MAY 2017

## Seasonal variability of the hydrogen exosphere of Mars

J. S. Halekas<sup>1</sup> <sup>1</sup>Department of Physics and Astronomy, University of Iowa, Iowa City, Iowa, USA

**Abstract** The Mars Atmosphere and Volatile Evolution (MAVEN) mission measures both the upstream solar wind and collisional products from energetic neutral hydrogen atoms that precipitate into the upper atmosphere after their initial formation by charge exchange with exospheric hydrogen. By computing the ratio between the densities of these populations, we derive a robust measurement of the column density of exospheric hydrogen upstream of the Martian bow shock. By comparing with Chamberlain-type model exospheres, we place new constraints on the structure and escape rates of exospheric hydrogen, derived from observations sensitive to a different and potentially complementary column from most scattered sunlight observations. Our observations provide quantitative estimates of the hydrogen exosphere with nearly complete temporal coverage, revealing order of magnitude seasonal changes in column density and a peak slightly after perihelion, approximately at southern summer solstice. The timing of this peak suggests either a lag in the response of the Martian atmosphere to solar inputs or a seasonal effect driven by lower atmosphere dynamics. The high degree of seasonal variability implied by our observations suggests that the Martian atmosphere and the thermal escape of light elements depend sensitively on solar inputs.

**Plain Language Summary** We utilize a new technique to measure the density of hydrogen escaping into space from Mars, allowing us to observe the variability of hydrogen around Mars over a full Martian year. We find that the current escape of hydrogen from Mars varies dramatically over the Martian year, suggesting a sensitive dependence of the atmosphere and the escape of hydrogen on the input of energy from the Sun, as well as a possible influence of seasonally varying weather patterns. Understanding the present-day and historical hydrogen escape from Mars is crucial to solving the problem of how Mars was transformed from an early warm wet state to the cold dry planet we see today. Our results provide a quantitative data set with good temporal coverage which is complementary to other measurements of Martian hydrogen and which provides important new constraints on models of the Martian atmosphere.

## 1. Introduction

The escape of atmospheric gases to space may have played a key role in transforming Mars from a warm and wet early state to its current cold dry condition. The Mars Atmosphere and Volatile Evolution (MAVEN) mission [Jakosky *et al.*, 2015] was designed to study atmospheric escape, which occurs through a variety of channels, with the dominant loss process(es) for each species depending primarily on mass and photochemical interactions. For the lightest species, notably atomic and molecular hydrogen, a thermal distribution of velocities includes an appreciable fraction of particles with escape velocity, and thermal (Jeans) escape therefore plays an important role in their loss.

The ballistic motion of hydrogen atoms above the exobase results in the formation of an extended exosphere or “corona” observable in ultraviolet (UV) scattered Lyman  $\alpha$  sunlight [Anderson, 1974; Anderson and Hord, 1971; Chaufray *et al.*, 2008; Feldman *et al.*, 2011; Chaffin *et al.*, 2015]. By fitting coronal observations to an exospheric model, one can estimate the loss rate of hydrogen from Mars. These observations return only the total column density along a line of sight, resulting in some ambiguity in derived escape rates [Chaffin *et al.*, 2014; Bhattacharyya *et al.*, 2017]. Hydrogen pickup ions [Dubinin *et al.*, 2006; Yamauchi *et al.*, 2015; Rahmati *et al.*, 2017], waves at the hydrogen cyclotron frequency [Bertucci *et al.*, 2013; Romanelli *et al.*, 2016], energetic neutral atoms from charge exchange [Futaana *et al.*, 2006; Gunell *et al.*, 2006], and their collisional products [Halekas *et al.*, 2015b, 2017] also provide more indirect information about the hydrogen exosphere.

Recent observations have revealed a high degree of variability in the hydrogen exosphere [Chaffin *et al.*, 2014; Clarke *et al.*, 2014, 2017; Yamauchi *et al.*, 2015; Bhattacharyya *et al.*, 2015; Romanelli *et al.*, 2016;

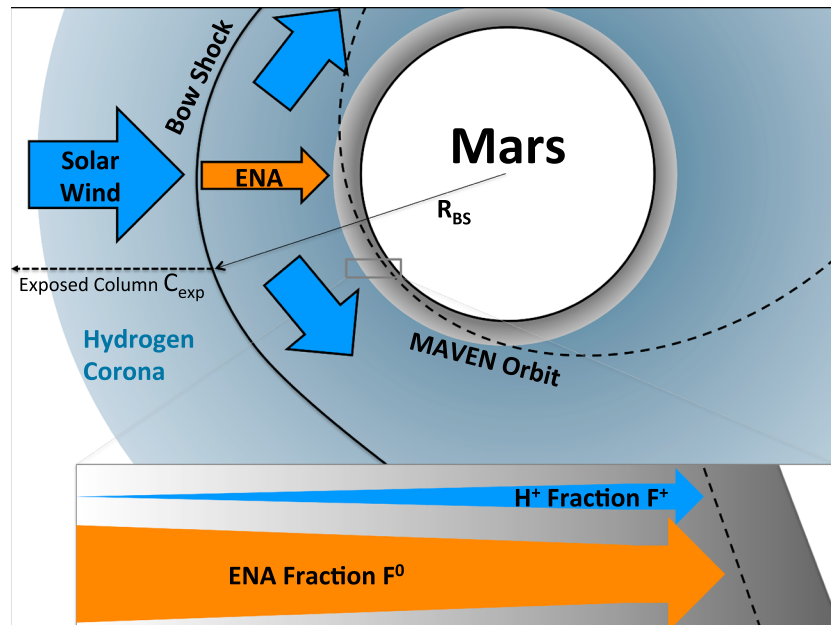


**Figure 1.** Schematic of penetrating protons, which are the charged fraction  $F^+$  of the collisional products of hydrogen energetic neutral atoms (ENAs) created by solar wind charge exchange with the hydrogen corona of Mars, as measured by MAVEN in the upper atmosphere.

*Rahmati et al., 2017; Halekas et al., 2017*], with higher column densities typically observed near perihelion and lower densities near aphelion. However, many of these observations have incomplete temporal coverage, and uncertainties in data inversion make it challenging to translate observations of seasonal variability into quantitative estimates of escape flux. As a result, questions remain about the exact form of the seasonal variability, the mechanism(s) responsible for creating this variability, and the implications for escape [*Chaufray et al., 2015; Chaffin et al., 2017*]. In this manuscript, we present observations from the Solar Wind Ion Analyzer (SWIA) on MAVEN [*Halekas et al., 2015a, 2017*] that provide a sensitive measurement of the high-altitude hydrogen corona along a different column than UV observations, with good temporal coverage over the Martian year.

## 2. Precipitating Hydrogen Observations

Thanks to Mars' weak gravity and diminutive magnetosphere, its hydrogen exosphere extends well upstream of the bow shock. As a result, a portion of the incoming solar wind proton population can charge exchange with exospheric hydrogen, producing energetic neutral atoms (ENAs) with the same velocity as the solar wind but no net charge, which propagate unaffected by electromagnetic fields. ENA instruments cannot observe this population directly, given the difficulty of eliminating solar UV contamination, but Mars Express (MEX) has observed the portion of the ENAs that backscatter from the atmosphere [*Futaana et al., 2006*], as well as a smaller population of ENAs originating in the magnetosheath [*Gunell et al., 2006*].

MAVEN has observed products of collisions between these hydrogen ENAs and species in the upper atmosphere, some fraction of which produce  $H^+$  and  $H^-$  measurable by charged particle instruments [*Halekas et al., 2015b, 2017*]. These particles, which we refer to as "penetrating protons," retain the solar wind velocity in the upper atmosphere, before they undergo enough collisions to experience a high degree of scattering and/or energy loss. Penetrating protons provide a proxy measurement of the solar wind and also contain information about the hydrogen exosphere, since the fraction of solar wind protons converted to neutral form outside the bow shock depends on the column density of the corona exposed to the incidence of the solar wind.

To infer the properties of the hydrogen exosphere from penetrating proton observations, we take into account a number of physical processes, shown in schematic form in Figure 1, and expressed below in a generalized equation (equation (1)).

$$N_{\text{pen}}(r) = N_{\text{sw}} \times \sigma_H(V_{\text{sw}}) \times C_{\text{exp}}(R_{\text{BS}}(N_{\text{sw}}, V_{\text{sw}}, \text{EUV})) \times F^+(r, V_{\text{sw}}) \quad (1)$$

The density of penetrating protons  $N_{\text{pen}}$  observed at radius  $r$  in the upper atmosphere depends on the density of the solar wind  $N_{\text{sw}}$ , the H-H<sup>+</sup> charge exchange cross section  $\sigma_H$  (which depends on the solar wind speed  $V_{\text{sw}}$ ), the exposed exospheric column density  $C_{\text{exp}}$ , which depends on the bow shock position  $R_{\text{BS}}$  (a function of solar wind and extreme ultraviolet (EUV) flux), and the fraction of precipitating ENAs converted to positively charged hydrogen  $F^+$ . This fraction depends on the electron stripping cross section  $\sigma_{01}$  and the charge exchange cross section  $\sigma_{10}$  (which depend on  $V_{\text{sw}}$ ) for hydrogen collisions with neutral atmospheric particles. In principle, these cross sections are a weighted sum over all particles that precipitating hydrogen collides with in the upper atmosphere; however, we only utilize CO<sub>2</sub> cross sections since these dominate the interaction. Given a neutral density profile  $n_n(r)$ , the charged and neutral precipitating fractions  $F^+$  and  $F^0$  satisfy coupled differential equations.

$$\frac{dF^+}{dr} = [\sigma_{01}F^0 - \sigma_{10}F^+]n_n(r) \quad \frac{dF^0}{dr} = [\sigma_{10}F^+ - \sigma_{01}F^0]n_n(r) \quad (2)$$

Given the initial conditions  $F^0(\infty) = 1$ ,  $F^+(\infty) = 0$ , equation (2) has solutions that converge to an equilibrium charged fraction:

$$F_{\text{eq}}^+ = \frac{\sigma_{01}(V_{\text{sw}})}{\sigma_{01}(V_{\text{sw}}) + \sigma_{10}(V_{\text{sw}})} \quad (3)$$

Based on the H-CO<sub>2</sub> cross sections from *Van Zyl et al.* [1978] and *Lindsay et al.* [2005], we expect an equilibrium charged fraction  $F_{\text{eq}}^+$  of ~4–15% for typical solar wind speeds, with higher charged fraction for larger speed. The neutral column density required for convergence is  $\sim 1/(\sigma_{01} + \sigma_{10})$  or  $\sim 10^{15} \text{ cm}^{-2}$  for typical solar wind speed. Some fraction of collisions also results in electron attachment, but we neglect these branching ratios since observations indicate negative fractions an order of magnitude below positive fractions [*Halekas et al.*, 2015b]. We also do not attempt the effects of remanent crustal magnetic fields, which might affect the precipitating flux at low altitude. Empirically, we have found no clear observational difference between measurements made in regions with strong crustal fields and those made in regions with no strong crustal fields.

From an observational standpoint, we wish to select observations from a low enough altitude that the ratio of charged to neutral hydrogen has converged sufficiently close to  $F_{\text{eq}}^+$  to allow us to invert the measurement of  $N_{\text{pen}}$  to obtain reliable information about the remaining terms in equation (1) but at a high enough altitude that collisions have not resulted in appreciable scattering and/or energy loss, so that  $V_{\text{pen}} \sim V_{\text{sw}}$  and we have a reliable measure of the solar wind speed.

Figure 2 shows penetrating proton observations from MAVEN SWIA. Each data point represents a background-subtracted moment of the portion of the ion distribution within 45° of the antisunward direction and with energies of 200–4000 eV. We include only measurements at altitudes below 250 km and in the ionosphere (to minimize direct access by magnetosheath protons) and only observations with peak count rates greater than 3 times the average count rate over the selected energy range and a consistent speed over the entire periapsis segment (to eliminate precipitating heavy ions, which typically have broader energy distributions and/or variable energies over an orbit).

Figure 2 reveals considerable variability in penetrating proton density with both time and altitude but with some consistent trends. Densities consistently increase with decreasing altitude down to a radius of ~3560 km, consistent with the expected altitude dependence of the charged fraction  $F^+(r)$  from equation (2). The peak penetrating density occurs at slightly different altitudes for different time periods, as expected given the seasonal variation of the neutral atmosphere [*Bougher et al.*, 2017]. Altitude coverage also varies, since MAVEN science operations target a specific neutral density range at periapsis. This altitude-time

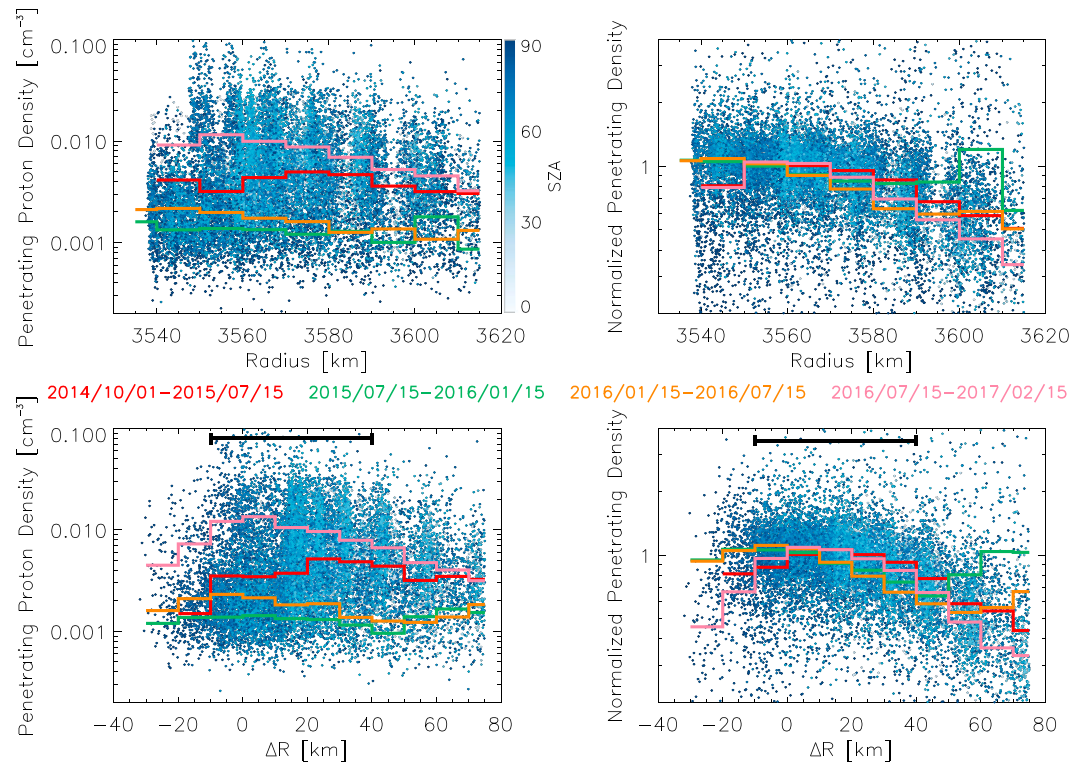


**Figure 2.** Penetrating proton densities measured by SWIA. (top row) Penetrating densities as a function of planetocentric radius. (bottom row) Densities as a function of  $\Delta R$ , the height above the point with expected column density equal to that at a subsolar radius of 3540 km (assuming a neutral scale height of 10 km). (left column) Measured densities and (right column) densities normalized on an orbit-by-orbit basis by the average density for  $-10 < \Delta R < +40$  km (range shown by solid black bars). The blue scale indicates the solar zenith angle (SZA) of individual measurements. The colored lines show medians for four intervals during the MAVEN mission, as indicated in the central figure legend.

convolution particularly affects our first time interval, which spans a broad range of conditions. Penetrating proton densities decrease at the lowest altitudes sampled by MAVEN, as collisions scatter and remove energy from the precipitating hydrogen. This drop appears mainly at high solar zenith angle (SZA), as expected given the larger column densities. A shifted radius  $\Delta R$  that partially takes into account such projection effects better organizes the observations. After normalizing each orbit, we find a reasonably flat plateau for all observations at  $\Delta R$  of  $-10$  to  $+40$  km, corresponding to  $F_{eq}^+$ . Though normalized altitude profiles vary slightly with time (due to atmospheric variability), within this selected range we obtain a reliable measurement of  $F_{eq}^+$  that we can compare across epochs and SZA. We utilize orbit-averaged values from this  $\Delta R$  range in all subsequent analyses.

Solar wind protons charge exchange with exospheric hydrogen both upstream in the solar wind and in the magnetosheath. Magnetosheath protons have a broader distribution of velocities, reducing access for their charge exchange products to the upper atmosphere. They also have lower energies, which reduces  $F^+$ . However, they encounter higher densities of exospheric hydrogen, which increases the ENA production rate. As a result of the interaction of solar wind and magnetosheath protons with the hydrogen exosphere, a typical penetrating proton spectrum has a narrow peak derived from the ENAs produced by charge exchange in the solar wind but also a component with lower amplitude but broader energy and angular width produced by charge exchange in the magnetosheath [e.g., Halekas et al., 2015b, Figures 2 and 4]. In this manuscript, we wish to focus only on the component produced in the solar wind. One can identify this component by manually finding the break in the penetrating proton energy and angular distribution between the narrow solar wind-produced component and the broader magnetosheath-produced component, removing the nonsolar wind-produced wings of the distribution and integrating over only those in the main peak. The separation is not exact, since some fraction of magnetosheath-produced and solar wind-produced ENAs can have the

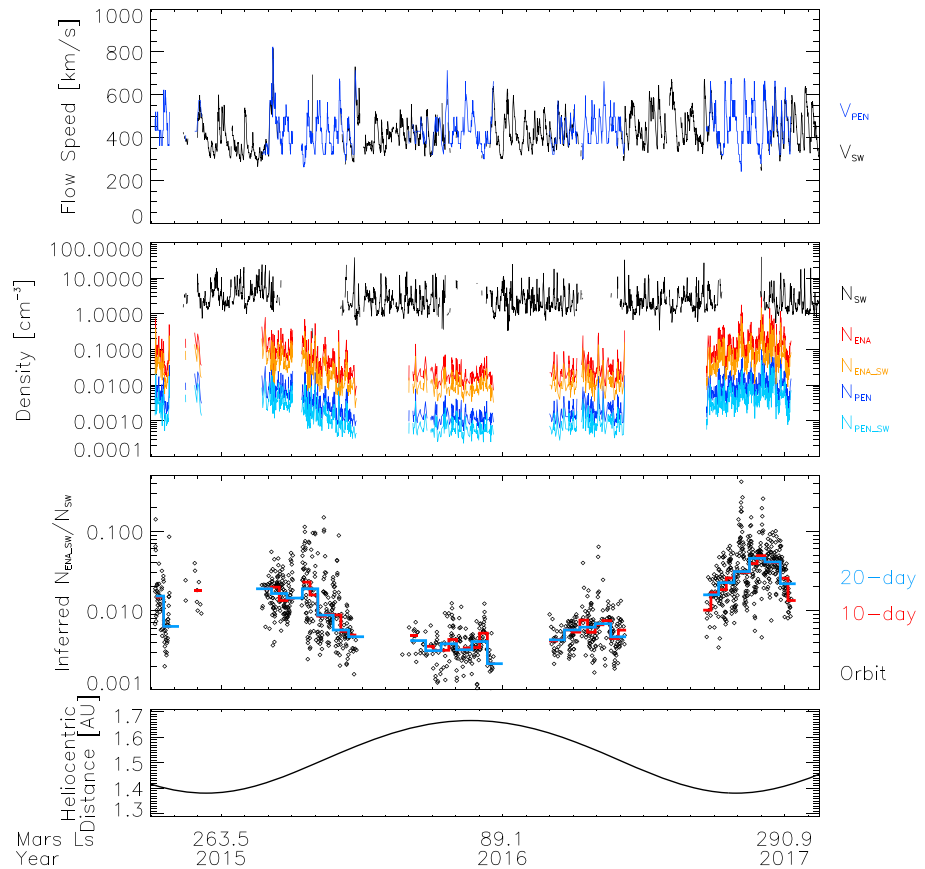


**Figure 3.** The flow speed and density of populations measured by SWIA. (first panel) Orbit-averaged values of measured solar wind speed and speed inferred from penetrating protons. (second panel) Orbit-averaged values of measured solar wind density, total penetrating proton density and that produced by charge exchange in the solar wind, and the corresponding ENA densities derived from equation (3). (third panel) The inferred fraction of solar wind protons converted to energetic neutral atoms (ENAs) outside of the bow shock, with individual orbit averages indicated by diamonds and colored lines showing 10 day and 20 day medians. During time periods when MAVEN does not sample the upstream solar wind, we utilize a smooth interpolation between the median values observed before and after the coverage gap.

same energy and angle; however, we estimate that the separation is accurate to the 10% level. This process proved difficult to automate reliably, so we estimated the solar wind component by conducting a detailed investigation of a sample of 20 orbits, drawn randomly from the entire mission (and thus not biased by season). The portion of the penetrating proton density produced by charge exchange in the solar wind for these 20 orbits varied from 38 to 60%, with a mean of 47%, a standard deviation of 6%, and a weak positive dependence on solar wind ram pressure. The dependence on solar wind ram pressure conforms to expectations, since high ram pressures compress the bow shock, exposing more of the exosphere to the direct impact of the solar wind. The recovery of this expected trend lends confidence in our separation procedure. Using the results from our random sample as a guide, we then scale all the orbit-averaged values from Figure 2 using a best fit linear equation  $N_{pen\_sw} = N_{pen} \times (0.45 + 5.5 \times 10^{-6} \times N_{pen} V_{pen}^2)$  to estimate the densities of the fraction of penetrating protons produced in the upstream solar wind.

Figure 3 shows SWIA observations of penetrating protons measured at periapsis and solar wind protons measured far from periapsis. Given the elliptical MAVEN orbit, these two sets of observations only overlap for brief periods when the orbit lies near the dawn-dusk plane. During these periods of overlap, solar wind speeds measured directly and inferred from penetrating protons match closely, lending confidence in the data reduction. The solar wind had slightly higher median densities in late 2014 and early 2015, near perihelion and closer to solar maximum, but otherwise maintained a relatively constant median value, with order of magnitude variability around that median. The penetrating proton densities have a similar envelope of

variability, but their median densities vary by an order of magnitude, with higher densities near perihelion than near aphelion (as reported by *Halekas et al.* [2017]). Given the relatively constant median solar wind, this variability must result from changes in the exposed column density  $C_{\text{exp}}$  of the hydrogen exosphere outside of the bow shock.

We utilize  $F_{\text{eq}}^+$  from equation (3), assuming  $V_{\text{sw}} = V_{\text{pen}}$ , to convert the penetrating proton densities  $N_{\text{pen\_sw}}$  to inferred ENA densities  $N_{\text{ENA\_sw}}$ . Orbit-averaged  $N_{\text{ENA\_sw}}/N_{\text{sw}}$  ratios display a high degree of variability, particularly during time periods when we do not directly observe the solar wind and have to extrapolate the solar wind density to estimate the ratio. However, by taking median values over longer time ranges, we minimize the effect of solar wind streams and other short-term sources of variability that do not represent real changes in the exosphere. We note that this averaging procedure also obscures any short-duration variability in the exosphere, and therefore our results cannot reveal short-term changes in the exosphere but only longer-term trends. Twenty-day medians work best at removing short-term variability, and we use these values in subsequent analyses. The inferred fraction of solar wind protons converted to ENAs outside the bow shock varies from ~0.5 to 5% over the mission. These measured values compare favorably to the 1–3% predicted by *Kallio et al.* [1997]. Since the same instrument measures both the upstream and penetrating populations, our estimate of this ratio remains robust independent of absolute calibrations.

### 3. Derived Exospheric Hydrogen Distribution and Escape Rates

We utilize the ratio between the density of ENAs  $N_{\text{ENA\_sw}}$  produced by charge exchange in the solar wind and the upstream density  $N_{\text{sw}}$  to determine the column density of hydrogen  $C_{\text{exp}}$  upstream of the bow shock. We use cross sections from *Barnett et al.* [1990] for  $\sigma_H(V_{\text{sw}})$  and perform a simple division to find  $C_{\text{exp}}$  for each orbit from the quantities determined in section 2. Figure 4 shows 20 day medians of  $C_{\text{exp}}$ .

In order to use  $C_{\text{exp}}$  values to retrieve an estimate of the exospheric hydrogen distribution, we must estimate the bow shock location  $R_{\text{BS}}$  upstream of the MAVEN periapsis to determine the spatial extent of the exosphere extending upstream. This problem is mildly nonlinear, since penetrating proton densities depend on both upstream parameters and  $R_{\text{BS}}$ , which itself depends on upstream parameters. Luckily, we can utilize periods of overlapping upstream and periapsis measurements to calibrate our method. After accounting for the observed long-term trends, we use these overlap periods to relate the upstream density  $N_{\text{sw}}$  to the measured penetrating density  $N_{\text{pen}}$  on an orbit-by-orbit basis, using an ad hoc correction factor that depends on the solar wind ram pressure raised to the power  $-0.31$ . This procedure provides an estimate that has a correlation coefficient of 0.81 and a one-to-one trend with the measured value of the upstream density during periods of overlap. In principle, the correction factor contains information about the hydrogen distribution and its variation with altitude; however, we use it only to estimate  $N_{\text{sw}}$  for orbits when we cannot directly measure it. Next, given estimates of the solar wind density and velocity and measured solar EUV fluxes from Extreme UltraViolet Monitor [*Eparvier et al.*, 2015], we use the results of *Halekas et al.* [2017] to extrapolate the bow shock radius  $R_{\text{BS}}$  upstream of the periapsis location for each orbit. Figure 4 shows that the solar wind variability mostly affects the shock location on short timescales of a few days, with this variability largely removed by taking 20 day medians (therefore, the correction factor described above has very little effect on the derived long-term trends). The EUV input influences the shock position on longer timescales, with the effect on  $R_{\text{BS}}$  most apparent for the first ~4–5 months of the MAVEN mission, when Mars experienced the largest EUV fluxes. In addition, the radius  $R_{\text{BS}}$  of the conical shock surface upstream of periapsis varies due to the orbit precession, leading to an additional medium-term periodicity with a roughly 3 month timescale.

Given the upstream bow shock location  $R_{\text{BS}}$ , we can forward model the exposed column density corresponding to any assumed hydrogen distribution, utilizing both the radius and solar zenith angle to determine the total integrated model column density upstream of the observation point. We utilize a standard Chamberlain form [*Chamberlain*, 1963] with no satellite orbits populated and compare the modeled values to the measured  $C_{\text{exp}}$  for each orbit to derive exospheric solutions that match the observed values. Figure 4 shows 20 day median values of two sets of exospheric solutions that match the observations, for a range of constant exobase temperatures and for a range of constant exobase densities. We display solutions for temperatures up to 800 K for ease of comparison to previous work [*Chaffin et al.*, 2014; *Bhattacharyya et al.*, 2015], though

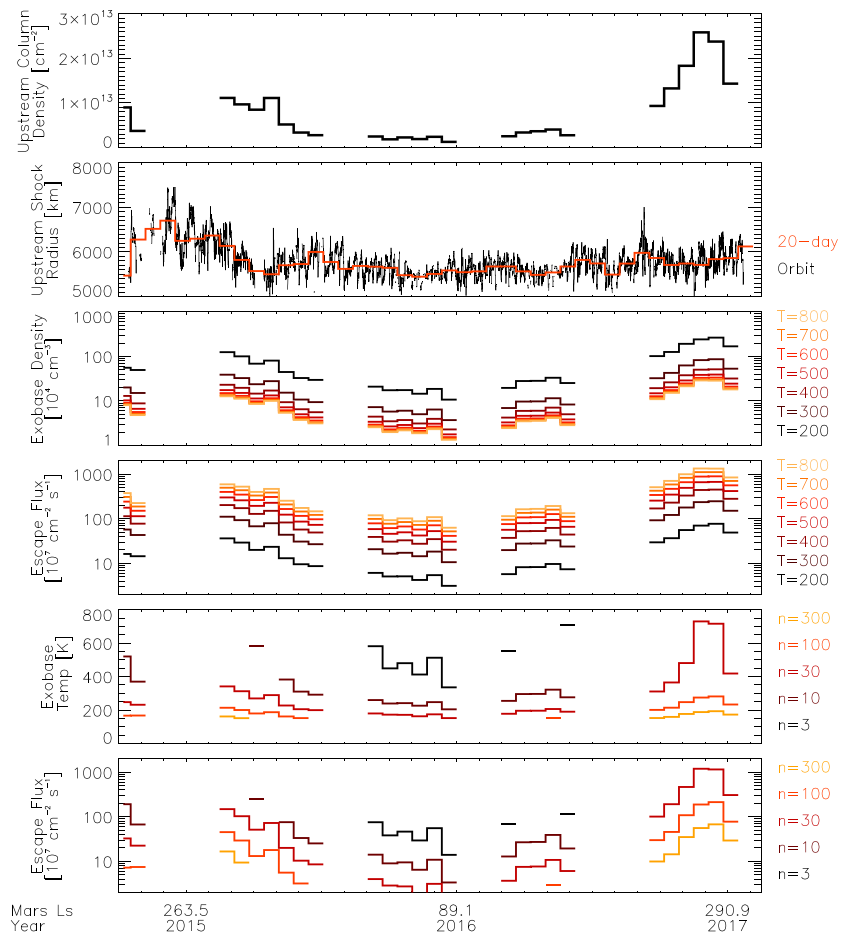


**Figure 4.** Derived solutions for Martian hydrogen exosphere structure and escape rates. (top panel) The upstream column density  $C_{\text{exp}}$  derived from our measurements. (second panel) The estimated bow shock radius  $R_{\text{BS}}$ . (third to sixth panels) The parameters of Chamberlain-type exospheric solutions consistent with the observations, for constant exobase temperatures (colored labels indicate values in kelvin) and for constant exobase densities (colored labels indicate values in units of  $10^4 \text{ cm}^{-3}$ ), and the corresponding hydrogen escape fluxes.

exobase temperatures above 400 K appear unlikely. One can generate arbitrary solutions with variations in both temperature and density by interpolating between these cases.

Near aphelion we require exobase densities of  $\sim 1\text{--}30 \times 10^4 \text{ cm}^{-3}$  to match the observations, assuming exobase temperatures of 200–800 K. These correspond to escape fluxes of  $3\text{--}100 \times 10^7 \text{ cm}^{-2} \text{ s}^{-1}$ . Near perihelion we require exobase densities of  $\sim 20\text{--}300 \times 10^4 \text{ cm}^{-3}$ , corresponding to escape fluxes of  $50\text{--}1000 \times 10^7 \text{ cm}^{-2} \text{ s}^{-1}$ , to match the observations. Our observations cover a full Mars year (with some gaps) and take place during the declining phase of a weak solar cycle, approaching solar minimum in the last year of observations.

Our derived values compare favorably to previous observations. *Anderson and Hord* [1971] found exobase densities of  $3 \times 10^4 \text{ cm}^{-3}$  for a 350 K exosphere at a Mars solar longitude of  $L_S \sim 200$  near solar maximum. *Chaufray et al.* [2008] found exobase densities of  $\sim 10\text{--}40 \times 10^4 \text{ cm}^{-3}$  for a 200–250 K exosphere at  $L_S \sim 180$  in the declining phase of the solar cycle. *Feldman et al.* [2011] found an exobase density of  $\sim 25 \times 10^4 \text{ cm}^{-3}$  for a 200 K exosphere at  $L_S \sim 190$  near solar minimum. The most comparable period covered by our observations spans March–June 2016, during which we infer exobase densities of  $6\text{--}30 \times 10^4 \text{ cm}^{-3}$  for temperatures of 200–400 K.

Recent observations from MEX and the Hubble Space Telescope (HST) have revealed seasonal variability in the hydrogen density and escape flux. *Chaffin et al.* [2015] used MEX observations to derive exobase

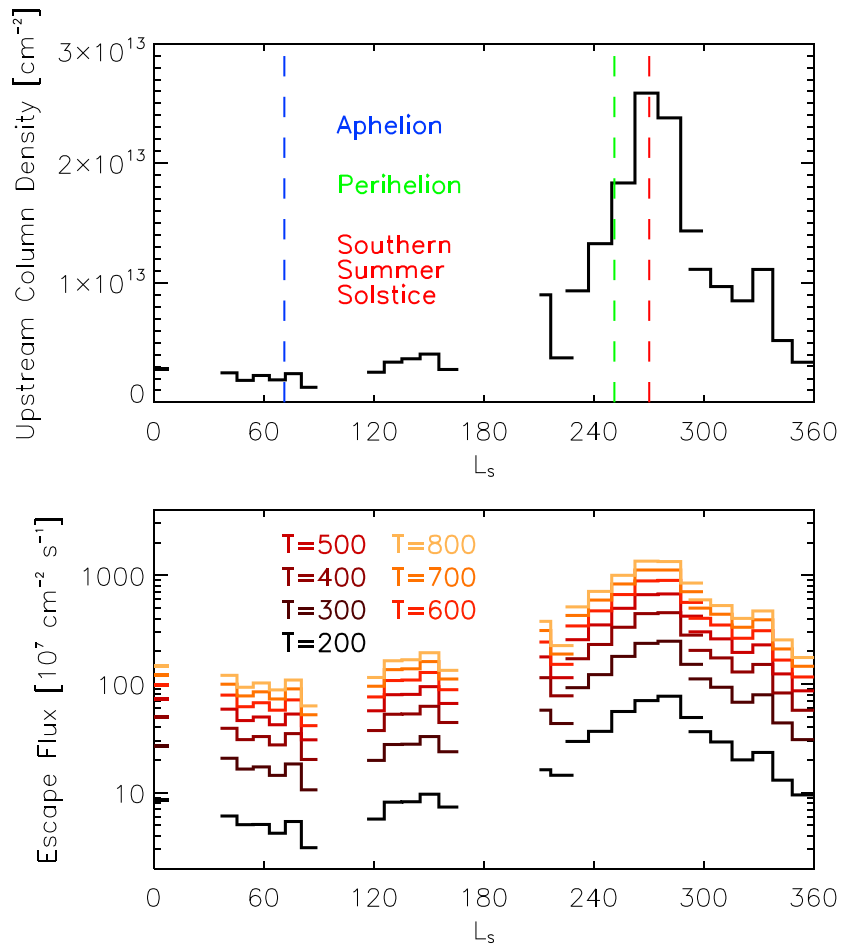


**Figure 5.** Inferred exospheric hydrogen column densities upstream of the bow shock and derived hydrogen escape fluxes for different assumed exobase temperatures, as a function of Mars solar longitude  $L_S$ .

densities of  $\sim 2\text{--}100 \times 10^4 \text{ cm}^{-3}$  for exobase temperatures of 100–1600 K, corresponding to escape fluxes of  $\sim 1\text{--}500 \times 10^7 \text{ cm}^{-2} \text{ s}^{-1}$  for  $L_S = 270\text{--}10$  near solar minimum, approximately the same as the range covered by our solutions for the most comparable time period spanning February–June 2015 and with a similar trend. *Clarke et al.* [2014] used HST observations to derive exobase densities decreasing from  $5 \times 10^4$  to  $3.5 \times 10^4 \text{ cm}^{-3}$  for an exospheric temperature of 340 K for  $L_S = 331\text{--}345$  near solar minimum, a factor of 2 lower than our values for the same  $L_S$  range in May 2015. *Bhattacharyya et al.* [2015] expanded the HST study to include observations from 2014 near solar maximum, covering  $L_S = 138\text{--}232$ . They derived exobase densities increasing from  $2 \times 10^4$  to  $7 \times 10^4 \text{ cm}^{-3}$  for a 440 K exospheric temperature, smaller by a factor of 2 to 3 than our values for the same  $L_S$  range in 2016 (though this disagreement could result in part from the high assumed temperature). However, they found better fits to the observations for a two-component distribution, implying somewhat higher total densities and escape fluxes, in better agreement with our derived values.

Our results also compare favorably to other measurements of the hydrogen exosphere. For a constant exobase temperature, we infer an order of magnitude annual variation in exobase density and escape flux, qualitatively comparable to MEX observations of pickup ions [*Yamauchi et al.*, 2015] and Mars Global Surveyor and MAVEN observations of waves [*Bertucci et al.*, 2013; *Romanelli et al.*, 2016]. *Rahmati et al.* [2017] inverted MAVEN SWIA pickup ion measurements to derive an exosphere a factor of 2 less dense than that found by *Feldman et al.* [2011] at  $L_S = 88$  and a factor of 5 more dense at  $L_S = 255$ , also comparable to our results.

#### 4. Seasonal Variability of the Hydrogen Exosphere

The MAVEN observations from the SWIA instrument described in this paper provide one of the most complete records of variability in the hydrogen exosphere over the Martian year, as shown in Figure 5. With the observations made to date, we have obtained nearly complete seasonal coverage. Where observations from different years overlap, we find reasonable agreement, suggesting a relatively repeatable pattern of variability, at least during the current declining phase of the solar cycle. We find a clear peak in the inferred hydrogen column density at  $L_S \sim 263\text{--}288$ , roughly centered on Mars southern summer solstice at  $L_S = 270$  and slightly after Mars perihelion at  $L_S = 251$ . The timing of this peak suggests either a lag in the response of the upper atmosphere to solar input or a seasonal influence in addition to the direct effects of the solar EUV. At the peak, we infer an order of magnitude higher upstream exospheric hydrogen column density than near aphelion. For a constant exobase temperature, this would imply a similar level of variability in both exobase density and escape flux. Given varying exobase temperatures, the level of variability in the escape flux could prove either lower (given lower temperatures at the peak) or higher (given higher temperatures at the peak, which appears more plausible given observed thermospheric variation [Bougher *et al.*, 2017]).

The seasonal variability implied by our observations compares well with that measured in scattered Lyman  $\alpha$  sunlight, as described above in section 3. On the other hand, our observations suggest escape fluxes in excess of those predicted by some models. Krasnopolsky [2002] did not model seasonal variability but did model solar cycle variability. They predicted exobase densities ranging from 3 to 40  $\text{cm}^{-3}$  and anticorrelated temperatures of 200–350 K, resulting in nearly constant escape fluxes of  $\sim 20 \times 10^7 \text{ cm}^{-2} \text{ s}^{-1}$ . The solutions consistent with our observations could fit within these parameters at all times except near the peak, when even the minimum escape flux consistent with our observations exceeds those predictions by a factor of 4. Chaufray *et al.* [2015], meanwhile, predicted a roughly fivefold annual variation in escape rate, with the maximum at perihelion and higher peak rates at solar maximum. The predicted level of variability agrees to first order with our observations; however, for temperatures comparable to the model predictions, our observations suggest escape rates a factor of  $\sim 3\text{--}8$  higher than the predicted solar minimum escape rates.

The recent photochemical modeling work of Chaffin *et al.* [2017], who found that high-altitude water could lead to elevated hydrogen escape rates on relatively short timescales of weeks, provides a possible resolution. Recent MEX observations show surprisingly large concentrations of high-altitude water, with rapid temporal variations in water concentration and generally higher values in southern spring and summer [Maltagliati *et al.*, 2013]. These observations and the modeling of Chaffin *et al.* [2017] may provide a link between seasonal variability in the lower atmosphere, high-altitude water concentration, and elevated escape of hydrogen. Our observations, which provide some of the best coverage of the seasonal variability of the exosphere to date, may help prove or disprove these new models for hydrogen escape.

#### 5. Conclusions and Implications

The SWIA instrument on MAVEN measures both the upstream solar wind and the collisional products of ENAs produced in the Martian hydrogen corona. By measuring the ratio between the densities of different observed and inferred populations, we derive a measurement of the column of exospheric hydrogen upstream of the Martian bow shock. By comparing this value with Chamberlain-type exosphere models, we place constraints on exospheric structure and the escape rate of hydrogen from Mars. These observations provide good temporal coverage of the seasonal variation of the hydrogen exosphere, revealing a strong peak in column density slightly after perihelion, approximately at southern summer solstice.

While we have performed a complex analysis that takes many factors into account in an attempt to derive the most accurate numbers possible, we emphasize that the basic measurement is simple and robust and does not even require accurate absolute sensitivity calibrations. After averaging over short-term solar wind variability, our observations indicate roughly constant solar wind input, but the presence of charge exchange products that vary by an order of magnitude over the Mars year indicates significant variability in the exosphere. A number of factors may affect the quantitative accuracy of our results, including solar wind variability not removed by averaging, inaccurate determination of  $F_{\text{eq}}^+$  due to altitude coverage variations, SZA dependence, scattering, and/or energy loss, inaccurate estimates of the bow shock location  $R_{\text{BS}}$ , inaccurate collisional cross sections, charge exchange with species other than atomic hydrogen in the exosphere (of

secondary importance outside the bow shock), contributions from neutral solar wind produced by charge exchange with interplanetary hydrogen (an order of magnitude lower than our signal), the presence of particles on satellite orbits, and any departures from a Chamberlain-type exosphere (we consider this rather likely, given the results of Chaffin *et al.* [2015]). We do not expect any of these individual error terms to lead to more than a few tens of percent error in our results, and we would predict that they would have competing effects on the final result, but we cannot rule out the possibility that compounded errors could play a role. However, no error that we have considered could lead to seasonal variations at anywhere close to the level that we observe. Furthermore, our results compare favorably to other observations made during the same time period, as well as those made during comparable conditions.

Our observations have a number of implications for the Martian environment. The seasonal variability implied by our observations suggests a high degree of sensitivity of the Martian atmosphere and the thermal escape of light elements to solar inputs. To understand the history of Mars, we will need to take into account this sensitivity to conduct any extrapolation of the water loss from Mars over its lifetime. Our observations also have implications for the Mars-solar wind interaction. At times with the strongest hydrogen exosphere, our observations indicate that ~5% of the solar wind converts to ENAs before reaching the bow shock, with a commensurate rate of production of hydrogen pickup ions. These newly born pickup ions will significantly perturb the plasma environment upstream from Mars and may even change the structure of the bow shock and magnetosphere, with secondary implications for escape. The precipitating hydrogen ENA population, meanwhile, represents a source of energy to the upper atmosphere, potentially capable of heating the atmosphere and/or producing emission in the form of “proton aurora.” We can expect to find the strongest signatures of all these effects near southern summer solstice.

#### Acknowledgments

We acknowledge the MAVEN contract and NASA grant NNX16AO84G for support. All MAVEN data are available on the Planetary Data System (<https://pds.nasa.gov>).

#### References

- Anderson, D. E., Jr. (1974), Mariner 6, 7, and 9 ultraviolet spectrometer experiment: Analysis of hydrogen Lyman alpha data, *J. Geophys. Res.*, *79*, 1513–1518, doi:10.1029/JA079i010p01513.
- Anderson, D. E., Jr., and C. W. Hord (1971), Mariner 6 and 7 ultraviolet spectrometer experiment: Analysis of hydrogen Lyman-alpha data, *J. Geophys. Res.*, *76*, 6666–6673, doi:10.1029/JA076i028p06666.
- Barnett, C. F., H. T. Hunter, M. I. Kirkpatrick, I. Alvarez, C. Cisneros, R. A. Phaneuf (1990), Atomic data for fusion. Collisions of H, H<sub>2</sub>, He, and Li atoms and ions with atoms and molecules, Oak Ridge Natl. Lab., ORNL-6086/V1, Oak Ridge, Tenn.
- Bertucci, C., N. Romanelli, J. Y. Chaufray, D. Gomez, C. Mazelle, M. Delva, R. Modolo, F. González-Galindo, and D. A. Brain (2013), Temporal variability of waves at the proton cyclotron frequency upstream from Mars: Implications for Mars distant hydrogen exosphere, *Geophys. Res. Lett.*, *40*, 3809–3813, doi:10.1002/grl.50709.
- Bhattacharyya, D., J. T. Clarke, J.-L. Bertaux, J.-Y. Chaufray, and M. Mayyasi (2015), A strong seasonal dependence in the Martian hydrogen exosphere, *Geophys. Res. Lett.*, *42*, 8678–8685, doi:10.1002/2015GL065804.
- Bhattacharyya, D., J. T. Clarke, J.-L. Bertaux, J.-Y. Chaufray, and M. Mayyasi (2017), Analysis and modeling of remote observations of the Martian hydrogen exosphere, *Icarus*, *281*, 264–280.
- Bougher, S. W., et al. (2017), The structure and variability of Mars dayside thermosphere from MAVEN NGIMS and IUVS measurements: Seasonal and solar activity trends in scale heights and temperatures, *J. Geophys. Res. Space Physics*, *122*, 1296–1313, doi:10.1002/2016JA023454.
- Chaffin, M. S., J.-Y. Chaufray, I. Stewart, F. Montmessin, N. M. Schneider, and J.-L. Bertaux (2014), Unexpected variability of Martian hydrogen escape, *Geophys. Res. Lett.*, *41*, 314–320, doi:10.1002/2013GL058578.
- Chaffin, M. S., et al. (2015), Three-dimensional structure in the Mars H corona revealed by IUVS on MAVEN, *Geophys. Res. Lett.*, *42*, 9001–9008, doi:10.1002/2015GL065287.
- Chaffin, M. S., J. Deighan, N. M. Schneider, and A. I. F. Stewart (2017), Elevated atmospheric escape of atomic hydrogen from Mars induced by high-altitude water, *Nat. Geosci.*, doi:10.1038/ngeo2887.
- Chamberlain, J. W. (1963), Planetary coronae and atmospheric evaporation, *Planet. Space Sci.*, *11*, 901–960, doi:10.1016/0032-0633(63)90122-3.
- Chaufray, J. Y., J. L. Bertaux, F. Leblanc, and E. Quémerais (2008), Observation of the hydrogen corona with SPICAM on Mars Express, *Icarus*, *195*, 598–613, doi:10.1016/j.icarus.2008.01.009.
- Chaufray, J. Y., F. Gonzalez-Galindo, F. Forget, M. A. Lopez-Valverde, F. Leblanc, R. Modolo, and S. Hess (2015), Variability of the hydrogen in the Martian upper atmosphere as simulated by a 3D atmosphere–exosphere coupling, *Icarus*, *245*, 282–294.
- Clarke, J. T., J. L. Bertaux, J. Y. Chaufray, G. R. Gladstone, E. Quemerais, J. K. Wilson, and D. Bhattacharyya (2014), A rapid decrease of the hydrogen corona of Mars, *Geophys. Res. Lett.*, *41*, 8013–8020, doi:10.1002/2014GL061803.
- Clarke, J. T., et al. (2017), Variability of D and H in the Martian upper atmosphere observed with the MAVEN IUVS echelle channel, *J. Geophys. Res. Space Physics*, *122*, 2336–2344, doi:10.1002/2016JA023479.
- Dubinin, E., M. Fraenz, J. Woch, S. Barabash, R. Lundin, and M. Yamauchi (2006), Hydrogen exosphere at Mars: Pickup protons and their acceleration at the bow shock, *Geophys. Res. Lett.*, *33*, L22103, doi:10.1029/2006GL027799.
- Eparvier, F. G., et al. (2015), The solar extreme ultraviolet monitor for MAVEN, *Space Sci. Rev.*, *195*, 293–301, doi:10.1007/s11214-015-0195-2.
- Feldman, P. D., et al. (2011), Rosetta-Alice observations of exospheric hydrogen and oxygen on Mars, *Icarus*, *214*, 394–399, doi:10.1016/j.icarus.2011.06.013.
- Futaana, Y., et al. (2006), First ENA observations at Mars: ENA emissions from the Martian upper atmosphere, *Icarus*, *182*, 424–430.
- Gunell, H., et al. (2006), First ENA observations at Mars: Charge exchange ENAs produced in the magnetosheath, *Icarus*, *182*, 431–438, doi:10.1016/j.icarus.2005.10.027.

- Halekas, J. S., E. R. Taylor, G. Dalton, G. Johnson, D. W. Curtis, J. P. McFadden, D. L. Mitchell, R. P. Lin, and B. M. Jakosky (2015a), The solar wind ion analyzer for MAVEN, *Space Sci. Rev.*, *195*, 125–151.
- Halekas, J. S., et al. (2015b), MAVEN observations of solar wind hydrogen deposition in the atmosphere of Mars, *Geophys. Res. Lett.*, *42*, 8901–8909, doi:10.1002/2015GL064693.
- Halekas, J. S., et al. (2017), Structure, dynamics, and seasonal variability of the Mars-solar wind interaction: MAVEN solar wind ion Analyzer in-flight performance and science results, *J. Geophys. Res. Space Physics*, *122*, 547–578, doi:10.1002/2016JA023167.
- Jakosky, B. M., et al. (2015), The Mars Atmosphere and Volatile Evolution (MAVEN) mission, *Space Sci. Rev.*, doi:10.1007/s11214-015-0139-x.
- Kallio, E., J. G. Luhmann, and S. Barabash (1997), Charge exchange near Mars: The solar wind absorption and energetic neutral atom production, *J. Geophys. Res.*, *102*, 22,183–22,197, doi:10.1029/97JA01662.
- Krasnopolsky, V. A. (2002), Mars' upper atmosphere and ionosphere at low, medium, and high solar activities: Implications for evolution of water, *J. Geophys. Res.*, *107*(E12), 5128, doi:10.1029/2001JE001809.
- Lindsay, B. G., W. S. Yu, and R. F. Stebbings (2005), Cross sections for charge-changing processes involving kilo-electron volt H and H<sup>+</sup> with CO and CO<sub>2</sub>, *Phys. Rev. A*, *71*, 032705.
- Maltagliati, L., et al. (2013), Annual survey of water vapor vertical distribution and water-aerosol coupling in the Martian atmosphere observed by SPICAM/MEx solar occultations, *Icarus*, *223*, 942–962.
- Rahmati, A., et al. (2017), MAVEN measured oxygen and hydrogen pickup ions: Probing the Martian exosphere and neutral escape, *J. Geophys. Res. Space Physics*, *122*, 3689–3706, doi:10.1002/2016JA023371.
- Romanelli, N., et al. (2016), Proton cyclotron waves occurrence rate upstream from Mars observed by MAVEN: Associated variability of the Martian upper atmosphere, *J. Geophys. Res. Space Physics*, *121*, 11,113–11,128, doi:10.1002/2016JA023270.
- Van Zyl, B., H. Neumann, T. Q. Le, and R. C. Amme (1978), H + N<sub>2</sub> and H + O<sub>2</sub> collisions: Experimental charge-production cross sections and differential scattering calculations, *Phys. Rev. A*, *18*, 506–516.
- Yamauchi, M., et al. (2015), Seasonal variation of Martian pick-up ions: Evidence of breathing exosphere, *Planet. Space Sci.*, doi:10.1016/j.pss.2015.09.013.